

Received December 12, 2019, accepted December 24, 2019, date of publication December 27, 2019, date of current version January 7, 2020.

Digital Object Identifier 10.1109/ACCESS.2019.2962750

# A Clifford Analytic Signal-Based Breast Lesion Segmentation Method for 4D Spatial-Temporal DCE-MRI Sequences

LIANG WANG<sup>1</sup>, HAOCHENG SHEN<sup>1</sup>, JUN ZHANG<sup>1</sup>, YANCHUN ZHU<sup>2</sup>, AND CHENG JIANG<sup>1</sup>

<sup>1</sup>Tencent AI Lab, Shenzhen 518054, China

<sup>2</sup>Tencent Healthcare, Shenzhen 518057, China

Corresponding author: Cheng Jiang (tabjiang@tencent.com)

This work was supported by the grants from Key Area Research and Development Program of Guangdong Province, China (No. 2018B010111001) and the Science and Technology Program of Shenzhen, China (No. ZDSYS201802021814180).

**ABSTRACT** Dynamic contrast enhanced magnetic resonance imaging (DCE-MRI) has been increasingly used for lesion detection in breast cancer diagnosis for its capability to provide spatial-temporal information. However, the massive and complex 4D spatial-temporal DCE-MRI data make the diagnosis process lengthy and error-prone. Moreover, normal fibroglandular tissue is occasionally enhanced through background parenchymal enhancement (BPE), which can degrade the performance of current algorithms. We propose a new method using a 3D Clifford analytic signal (CAS) approach for breast lesion segmentation of DCE-MRI data. A 2D temporal image is constructed from all the 2D DCE-MRI slices at different scanning time points on a given transverse plane, according to the CAS approach. Then, a 3D Clifford temporal image (CTI) is constructed by successively stacking temporal images. The proposed CTI can distinguish lesion regions both visually and quantitatively compared to the traditional DCE-MRI subtraction image. Finally, we employ a fully convolutional network (FCN) model for breast lesion segmentation using the CTI as one of the inputs. Experimental results on an independent public dataset (TCIA QIN breast DCE-MRI) and a private household breast DCE-MRI dataset (TBD) show that the proposed method can achieve superior performance over current methods, both qualitatively and quantitatively.

**INDEX TERMS** Breast DCE-MRI, breast lesion segmentation, fully convolutional network, clifford analytic signal, clifford temporal image.

## I. INTRODUCTION

Dynamic contrast enhanced magnetic resonance imaging (DCE-MRI) is one of the most important imaging modalities for breast cancer diagnosis. It has been increasingly used, considering the enhancement kinetics on the 4D spatial-temporal DCE-MRI data can provide high sensitivity and accuracy for lesion detection in breast cancer diagnosis [1].

Although accurate detection or segmentation of lesions is not a prerequisite for cancer diagnosis [2]–[4], the lesion results allow interactive diagnosis and facilitate the use of diagnosis algorithms with fewer false positives. Early computer-aided techniques for lesion detection include region-growing algorithms [5], fuzzy c-means approaches [6], and level set methods [7]. These methods work well mainly on breast lesions with sharp borders [8]. To better exploit the information of DCE-MRI sequences,

it is necessary to deal with the background parenchymal enhancement (BPE), for which normal fibroglandular tissue is occasionally enhanced for some reasons (e.g., patient age and day of menstrual cycle). Because of BPE, lesions with low enhancement, such as non-mass lesions, can hardly be detected by these early methods, which usually adopt manually tuned parameters.

Deep learning-based methods offer better accuracy and reliability for breast lesion segmentation tasks [2]–[4], [9]. Although model parameters can be trained automatically, most approaches still have preprocessing problems, such as 2D/3D slice or region of interest (ROI) selection, mass-type and non-mass enhancement (NME) data selection, and time point selection of DCE-MRI sequences to produce the subtraction image.

For the problem of 2D/3D slice or ROI selection, Zhang et al. [10], [11] used a 2D-based slice-by-slice method for whole breast segmentation by a convolutional network on DCE-MRI and DWI sequences and used both 2D and 3D DCE-MRI data for breast tumor segmentation.

The associate editor coordinating the review of this manuscript and approving it for publication was Yakoub Bazi<sup>1</sup>.

Also, a 3D voxel-wise hierarchical lesion segmentation method was proposed via fully convolutional network (FCN) to obtain lesion segmentation probability maps with the help of a nipple landmark identification approach [12].

For the problem of mass-type and NME data selection, the analysis of NME is one of the difficulties of breast lesion segmentation, and several deep learning-based methods [8], [13] can only deal with the mass-type lesion segmentation problem. For NME lesion segmentation, Gallego-Otriz et al. [14] used a graph-modeling approach based on given 2D ROIs for feature representation of non-mass-like lesions. Illan et al. [9] adopted independent component analysis (ICA) for voxel feature extraction and a support vector machine (SVM) for classification of non-mass-like lesions. Dalmış et al. [15] used the spatial information on early-phase DCE-MRI sequences and the symmetry information of the two sides of the breast for both mass and NME lesion segmentation by convolutional neural networks (CNNs).

For the problem of DCE-MRI time point selection, although the data contain several temporal enhanced 3D sequences, few lesion-segmentation algorithms can be directly applied to all these temporal sequences. This is usually alleviated by applying the algorithms on a subtraction image obtained by subtracting two sequences before and after contrast injection. The subtraction image from the first post-contrast sequence and pre-contrast sequence of DCE-MRI was used in [16]. For segmentation, the breast ROI was first extracted from T1-weighted anatomical data, then ResNet [17] and Q-network [18] were used to obtain a focus of attention on the lesion ROI. In another study, Maicas et al. [19] segmented the lesion from a breast ROI of the DCE-MRI subtraction image by minimizing an energy function based on a CNN prior, mean shape, and piecewise constant Mumford Shah model [20]. Other methods, such as salient region proposition from a deep learning model, and a weakly label-based method, were proposed for malignant lesion segmentation in recent studies [21], [22]. These methods all use one time point of the post-contrast and pre-contrast DCE-MRI sequence to produce the subtraction image. However, one subtraction image cannot eliminate enhanced vessels and fibroglandular tissue because of BPE. The problem is somewhat alleviated based on the temporal gradient information by manually selecting one best time point of the DCE-MRI sequence [23], but manual selection is time-consuming.

Approaches with manual pre-selection of lesion ROI and type (mass and NME) are generally inconvenient in real clinical applications. Moreover, approaches that do not use multiple or sufficient time points of DCE-MRI sequences may overlook important temporal information for lesion segmentation [16], [19], [21]–[23]. An end-to-end framework that can fully utilize the temporal information from multiple DCE-MRI data to segment both mass-type and NME lesions is still lacking.

This paper makes two major contributions. First, we propose a 3D biquaternion Clifford analytic signal (CAS) approach and its realizable form for practical application. We further propose a 3D Clifford temporal image (CTI) construction method by applying the CAS to the 4D spatial-temporal DCE-MRI data, which can automatically combine all the temporal information of DCE-MRI sequences. Especially, we observe that the response of non-lesion tissues can be relatively suppressed from the 3D CTI. Second, we develop a parameter-free end-to-end framework with two successive FCNs for lesion segmentation that is suitable for both mass-type and NME data. The entire breast segmentation, from pre-contrast sequence by using FCN is implemented as the first step. Then the 3D CTI and the whole breast mask are combined as inputs to train another FCN for lesion segmentation. Our method outperformed current methods both qualitatively and quantitatively on a private dataset (224 patients) and public dataset (seven patients).

## II. METHODS

The decomposition property of analytic signals has been successfully applied to 2D ultrasound envelope detection [24] and myocardium motion estimation of 2D MRI images [25]. In this study, the decomposition property of a 3D complex analytic signal is adopted to extract the temporal information of 4D spatial-temporal DCE-MRI data. In this way, DCE-MRI sequences of all time points are taken into account in obtaining the 3D CTI data, which is suitable for breast lesion segmentation.

The general scheme of our method is shown in Fig. 1. First, the 4D DCE-MRI data are regrouped into several sets of 3D image data by a given transverse plane. Therefore, each 3D image data contains all time point slices of a fixed transverse plane, which are used as the input for the CAS approach. Hence, eight CAS elements of the input 3D data are split out by the CAS approach. Then, using one of the CAS elements, a 2D temporal image of the given transverse plane is constructed. Finally, we can obtain a 3D CTI from the input 4D DCE-MRI data by stacking all the 2D temporal images. Based on these CTI sequences, we train two successive FCNs. For the input DCE-MRI data, the ROI of the whole breast is first estimated from the pre-contrast sequence through the first FCN. Then the breast ROIs and the extracted 3D CTI are fed into the second FCN to get the lesion segmentation result.

### A. 1D AND 3D COMPLEX ANALYTIC SIGNAL

To understand our method, we will first review the complex analytic signal (AS) [26] for 1D and 3D cases. The complex AS of a 1D real signal  $f(t)$  can be presented as

$$\psi(t) = f(t) \star \left( \delta(t) + \frac{i}{\pi t} \right) = f(t) + iH\{f(t)\}, \quad (1)$$

where  $i$  is the complex imaginary part (*i.e.*,  $i^2 = -1$ ), and  $\star$  is the 1D convolution. The real part of  $\psi(t)$  is the input signal itself.  $H\{\cdot\}$  is the Hilbert transform, which represents the imaginary part of  $\psi(t)$ .

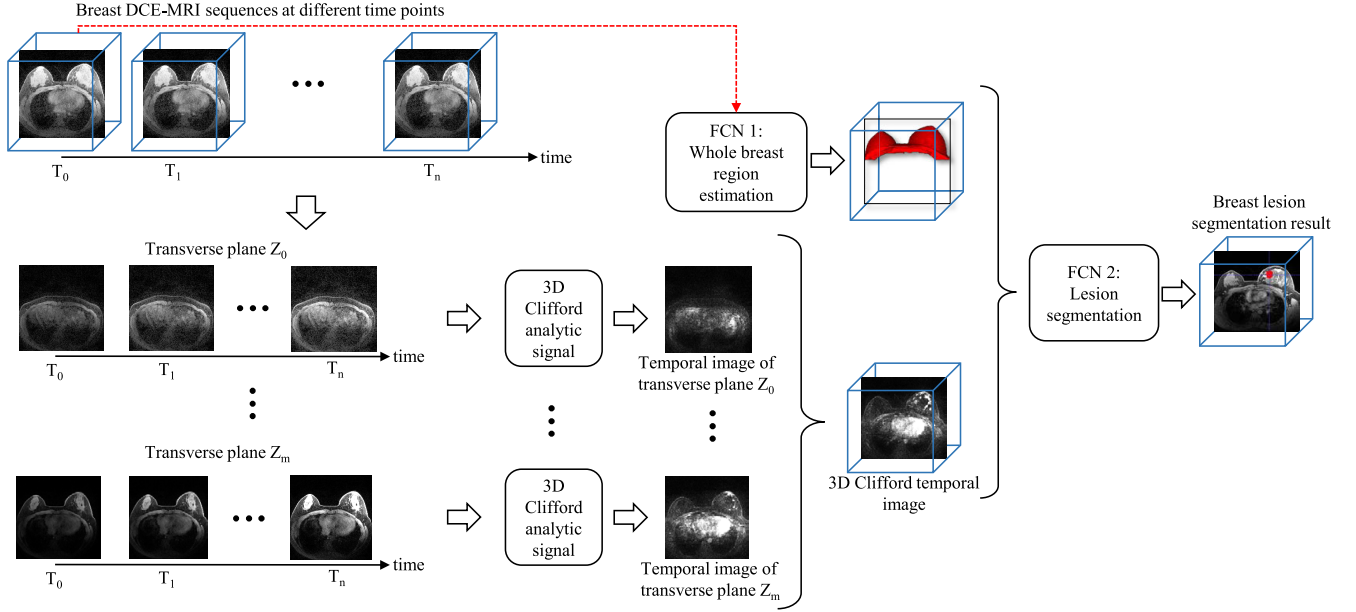


FIGURE 1. General scheme of the proposed method.

According to all the DCE-MRI sequences, the 2D images from all time points at a fixed transverse plane can be defined by a real signal  $f(x, y, t)$ , where  $x, y$  represent the image coordinates, and  $t$  is the time point. Based on the theory of the single-orthant analytic signal [26], the full spatial-temporal information of  $f(x, y, t)$  can be represented by four ASs:

$$\begin{aligned} \psi_1(x, y, t) &= f(x, y, t) \star \star \star \left\{ \left[ \delta(x) + \frac{i}{\pi x} \right] \left[ \delta(y) + \frac{i}{\pi y} \right] \left[ \delta(t) + \frac{i}{\pi t} \right] \right\}, \end{aligned} \quad (2)$$

$$\begin{aligned} \psi_2(x, y, t) &= f(x, y, t) \star \star \star \left\{ \left[ \delta(x) + \frac{i}{\pi x} \right] \left[ \delta(y) - \frac{i}{\pi y} \right] \left[ \delta(t) + \frac{i}{\pi t} \right] \right\}, \end{aligned} \quad (3)$$

$$\begin{aligned} \psi_3(x, y, t) &= f(x, y, t) \star \star \star \left\{ \left[ \delta(x) + \frac{i}{\pi x} \right] \left[ \delta(y) + \frac{i}{\pi y} \right] \left[ \delta(t) - \frac{i}{\pi t} \right] \right\}, \end{aligned} \quad (4)$$

$$\begin{aligned} \psi_4(x, y, t) &= f(x, y, t) \star \star \star \left\{ \left[ \delta(x) + \frac{i}{\pi x} \right] \left[ \delta(y) - \frac{i}{\pi y} \right] \left[ \delta(t) - \frac{i}{\pi t} \right] \right\}, \end{aligned} \quad (5)$$

where  $\psi(\cdot)$  are obtained from a single-orthant of Fourier spectra of  $f(x, y, t)$ , and  $\star \star \star$  represents 3D convolution. Taking  $\psi_1(x, y, t)$  as an example, we obtain

$$\begin{aligned} \psi_1(x, y, t) &= f(x, y, t) \star \star \star \left\{ \delta(x)\delta(y)\delta(t) + i\frac{\delta(x)\delta(y)}{\pi t} + i\frac{\delta(x)\delta(t)}{\pi y} \right. \\ &\quad \left. - \frac{\delta(x)}{\pi^2 yt} + i\frac{\delta(y)\delta(t)}{\pi x} - \frac{\delta(y)}{\pi^2 xt} - \frac{\delta(t)}{\pi^2 xy} - i\frac{1}{\pi^3 xyt} \right\} \end{aligned}$$

$$\begin{aligned} &= (f - H_{xy}\{f\} - H_{xt}\{f\} - H_{yt}\{f\}) \\ &\quad + i(H_x\{f\} + H_y\{f\} + H_t\{f\} - H\{f\}) \\ &= a_1 e^{i\varphi_1} = a_1 \cos \varphi_1 + ia_1 \sin \varphi_1, \end{aligned} \quad (6)$$

where  $H\{f\}$  is the total Hilbert transform of  $f(x, y, t)$ ;  $H_x\{f\}$ ,  $H_y\{f\}$ , and  $H_t\{f\}$  are the partial Hilbert transforms of  $f(x, y, t)$  for one direction of  $x, y$ , and  $t$ , respectively;  $H_{xy}\{f\}$ ,  $H_{xt}\{f\}$ , and  $H_{yt}\{f\}$  are the partial Hilbert transform of  $f(x, y, t)$  for two directions  $(x, y)$ ,  $(x, t)$ , and  $(y, t)$ , respectively; and  $a_1$  and  $\varphi_1$  are the modulus and phase, respectively, of the polar form of  $\psi_1$ .

Similarly, the other 3D ASs of the single-orthant of Fourier spectra defined in (3)-(5) are as follows:

$$\begin{aligned} \psi_2(x, y, t) &= (f + H_{xy}\{f\} - H_{xt}\{f\} + H_{yt}\{f\}) \\ &\quad + i(H_x\{f\} - H_y\{f\} + H_t\{f\} + H\{f\}) \\ &= a_2 e^{i\varphi_2} = a_2 \cos \varphi_2 + ia_2 \sin \varphi_2, \end{aligned} \quad (7)$$

$$\begin{aligned} \psi_3(x, y, t) &= (f - H_{xy}\{f\} + H_{xt}\{f\} + H_{yt}\{f\}) \\ &\quad + i(H_x\{f\} + H_y\{f\} - H_t\{f\} + H\{f\}) \\ &= a_3 e^{i\varphi_3} = a_3 \cos \varphi_3 + ia_3 \sin \varphi_3, \end{aligned} \quad (8)$$

$$\begin{aligned} \psi_4(x, y, t) &= (f + H_{xy}\{f\} + H_{xt}\{f\} - H_{yt}\{f\}) \\ &\quad + i(H_x\{f\} - H_y\{f\} - H_t\{f\} - H\{f\}) \\ &= a_4 e^{i\varphi_4} = a_4 \cos \varphi_4 + ia_4 \sin \varphi_4. \end{aligned} \quad (9)$$

Generally, we can observe that the Hilbert transforms and the phases and modulus of AS have a mathematical relation. Next, these formulations will be extended to 3D CAS.

## B. 3D CLIFFORD ANALYTIC SIGNAL

As discussed in section II-A, an AS is defined based on one imaginary unit  $i$ . In the framework of Clifford algebra, an AS can be called a 1D Clifford signal with one generator  $e_1$

(i.e.,  $e_1 = i$ ). We propose a 3D CAS under the framework of Clifford algebra with three generators.

### 1) DEFINITION OF 3D CAS IN CLIFFORD BIQUATERNION FORM

Based on the work in [27], Clifford biquaternions are used to define a 3D CAS. Three generators,  $e_1$ ,  $e_2$ , and  $e_3$ , are defined to generate eight elements of a full algebra:

$$\begin{aligned} [1, \quad i = e_2 e_3, \quad j = e_3 e_1, \quad k = e_1 e_2, \\ \epsilon = -e_1 e_2 e_3, \quad \epsilon i = e_1, \quad \epsilon j = e_2, \quad \epsilon k = e_3], \end{aligned} \quad (10)$$

with  $\epsilon^2 = 1$ ,  $e_1^2 = e_2^2 = e_3^2 = -1$ .

For a 3D input real signal  $f(x, y, t)$ , the 3D CAS can be defined in Clifford biquaternion form as

$$\begin{aligned} \psi_{cas}(x, y, t) \\ = f(x, y, t) \star \star \star \left\{ \left[ \delta(x) + \frac{e_1}{\pi x} \right] \left[ \delta(y) + \frac{e_2}{\pi y} \right] \left[ \delta(t) + \frac{e_3}{\pi t} \right] \right\}. \end{aligned} \quad (11)$$

Similar to (6), we develop  $\psi_{cas}(x, y, t)$  and obtain

$$\begin{aligned} \psi_{cas}(x, y, t) = f + iH_{yt}\{f\} + j(-H_{xt}\{f\}) + kH_{xy}\{f\} \\ + \epsilon(-H\{f\}) + \epsilon iH_x\{f\} + \epsilon jH_y\{f\} + \epsilon kH_t\{f\}, \end{aligned} \quad (12)$$

where  $e_1$ ,  $e_2$ , and  $e_3$  are the imaginary units related as in (10).

The eight elements constitute a biquaternion. The biquaternion form of the CAS separates the input signal into eight elements. It can be noticed that the element  $H_t\{f(x, y, t)\}$  with the imaginary unit  $\epsilon k$  in (12) is a partial Hilbert transform of  $f(x, y, t)$  for one direction of  $t$ . Therefore,  $H_t\{f(x, y, t)\}$  can be considered a kind of temporal information of  $f(x, y, t)$ . To apply  $H_t\{f(x, y, t)\}$  for DCE-MRI temporal image extraction, we deduce a practical way to obtain  $H_t\{f(x, y, t)\}$  by conventional Fourier transformation.

### 2) PRACTICAL REALIZATION OF DEFINITION OF 3D CAS IN CLIFFORD BIQUATERNION FORM

The polar form of AS in (6)-(9) can be obtained practically using a conventional Fourier transformation method. Further, all the elements of ASs and CAS can be represented by Hilbert transforms of the input signal. As a result, from (6)-(9) and (12), the 3D CAS can be represented by the modulus and phases of the four ASs:

$$\begin{aligned} \psi_{cas}(x, y, t) \\ = \frac{1}{4} [(a_1 \cos \varphi_1 + a_2 \cos \varphi_2 + a_3 \cos \varphi_3 + a_4 \cos \varphi_4) \\ + i(-a_1 \cos \varphi_1 + a_2 \cos \varphi_2 + a_3 \cos \varphi_3 - a_4 \cos \varphi_4) \\ + j(a_1 \cos \varphi_1 + a_2 \cos \varphi_2 - a_3 \cos \varphi_3 - a_4 \cos \varphi_4) \\ + k(-a_1 \cos \varphi_1 + a_2 \cos \varphi_2 - a_3 \cos \varphi_3 + a_4 \cos \varphi_4) \\ + \epsilon(a_1 \sin \varphi_1 - a_2 \sin \varphi_2 - a_3 \sin \varphi_3 + a_4 \sin \varphi_4) \\ + \epsilon i(a_1 \sin \varphi_1 + a_2 \sin \varphi_2 + a_3 \sin \varphi_3 + a_4 \sin \varphi_4) \\ + \epsilon j(a_1 \sin \varphi_1 - a_2 \sin \varphi_2 + a_3 \sin \varphi_3 - a_4 \sin \varphi_4) \\ + \epsilon k(a_1 \sin \varphi_1 + a_2 \sin \varphi_2 - a_3 \sin \varphi_3 - a_4 \sin \varphi_4)]. \end{aligned} \quad (13)$$

Hence we obtain

$$\begin{aligned} H_t\{f(x, y, t)\} \\ = \frac{1}{4}(a_1 \sin \varphi_1 + a_2 \sin \varphi_2 - a_3 \sin \varphi_3 - a_4 \sin \varphi_4). \end{aligned} \quad (14)$$

### C. 3D CLIFFORD TEMPORAL IMAGE

The DCE-MRI sequences of all time points can be defined as 4D data  $I(x, y, z, t)$ , where  $(x, y)$  represents the axis of the transverse plane,  $z$  is the position of the transverse plane, and  $t$  is the time point. A 3D CTI  $I_C(x, y, z)$  is calculated using CAS for lesion segmentation. Each transverse plane of  $I_C(x, y, z)$  is obtained from (14). Given a transverse plane  $z_m$ , we obtain the difference between the maximum and minimum voxel intensity on each position of  $(x, y)$  from  $H_t\{I(x, y, z_m, t)\}$  along the time axis:

$$\begin{aligned} I_C(x, y, z_m) = \max_{t \in [1, T_n]} \{H_t\{I(x, y, z_m, t)\}\} \\ - \min_{t \in [1, T_n]} \{H_t\{I(x, y, z_m, t)\}\}. \end{aligned} \quad (15)$$

To better illustrate the principle of the proposed CTI, we present an example in Fig. 2. Fig. 2(a) and (b) show example slices of  $I(x, y, z, t)$  and  $H_t\{I(x, y, z, t)\}$ , respectively, on two time points. The dashed arrows indicate the lesion ROIs on the slices from one side of the breast, and the solid arrows indicate the normal ROIs on the similar position from the other side. Fig. 2(c) and (d) show the time-intensity curves of a lesion ROI (dashed lines) and normal ROI (solid lines) from all time points. From the curves of the proposed CTI results in Fig. 2(d), we can find that the intensity of the lesion curve (dashed line) can be well distinguished from the curve (solid line) of a normal ROI. Examples of  $I_C(x, y, z_m)$  are shown in the first column of Fig. 3 and Fig. 4.

## III. EXPERIMENTS AND RESULTS

### A. DATASET

Two datasets were used in this study. What we will call the Tencent breast DCE-MRI (TBD) dataset was collected from more than 200 patients by our collaborating hospital from 2014 to 2018. What we will call QIN DCE is a public dataset with 20 studies of 10 patients from the Cancer Imaging Archive (TCIA) Quantitative Imaging Network (QIN) Breast DCE-MRI [28]. Data with surgery, non-visible lesions on DCE-MRI sequences, and sequences with very heavy bias fields or incomplete scanning were not considered. We used data of 224 patients in our TBD dataset and 12 studies of seven patients from QIN DCE for the experiments. From the TBD dataset, the training, validation, and test data were from 184, 20, and 20 patients, respectively. All the QIN DCE data were used as independent test data, which can validate the generalization of the proposed method. Specifically, for the TBD dataset, we had one pre-contrast time point and five post-contrast time points for each patient. They are the transverse plane images acquired from a Siemens Skyra 3T MRI scanner. The image size on each transverse plane was  $448 \times 448$ , with a pixel spacing of 0.8 mm. The



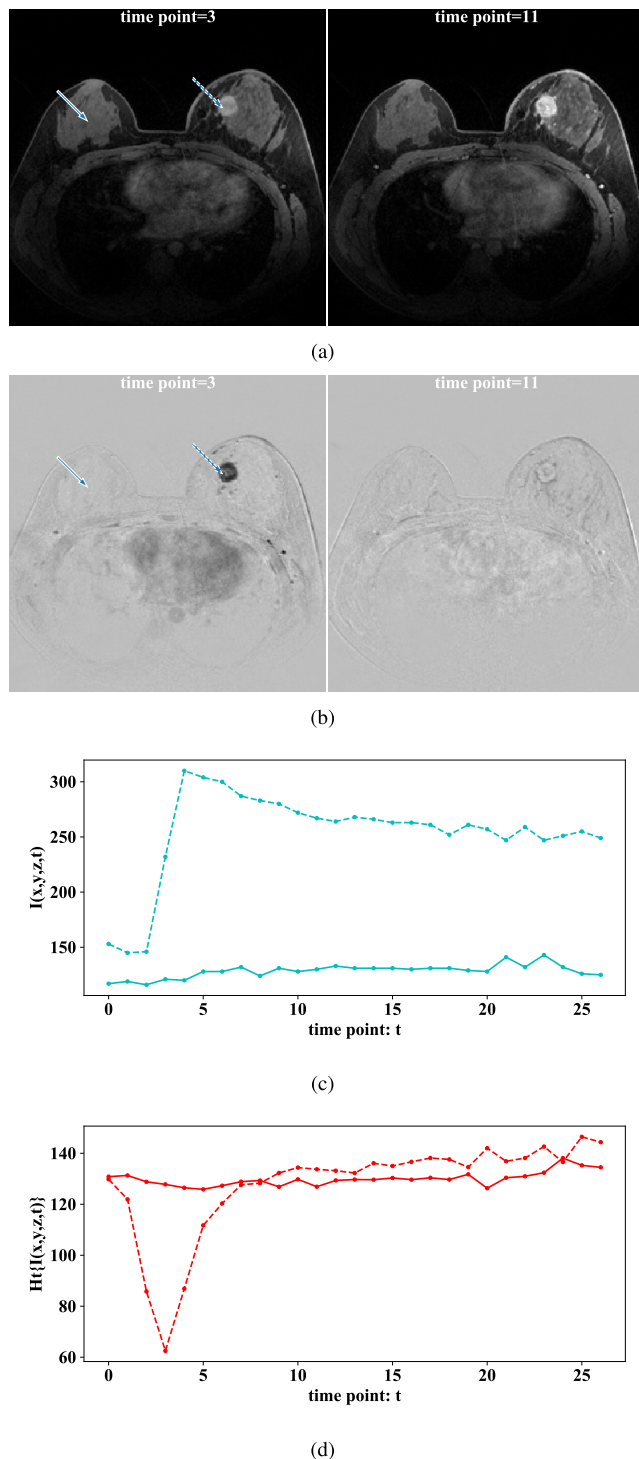


**FIGURE 2.** Case BC01\_2 of QIN DCE dataset. (a) two slices on different time points from DCE-MRI sequence data  $I(x, y, z, t)$ , and (b) from its partial Hilbert transform on direction  $t$ :  $H_t\{I(x, y, z, t)\}$ ; (c) time-intensity curves from DCE-MRI sequences, in cyan, and (d) from  $H_t\{I(x, y, z, t)\}$ , in red. The dashed lines correspond to the lesion ROI indicated by dashed arrows in (a) and (b). solid lines correspond to normal ROI indicated by solid arrow in (a) and (b).

number of transverse plane images from each sequence was around 80, with slice spacing ranging from 1.6 mm to 2 mm. The voxel-wise lesion annotations were performed by an experienced radiologist and reviewed by another radiologist.

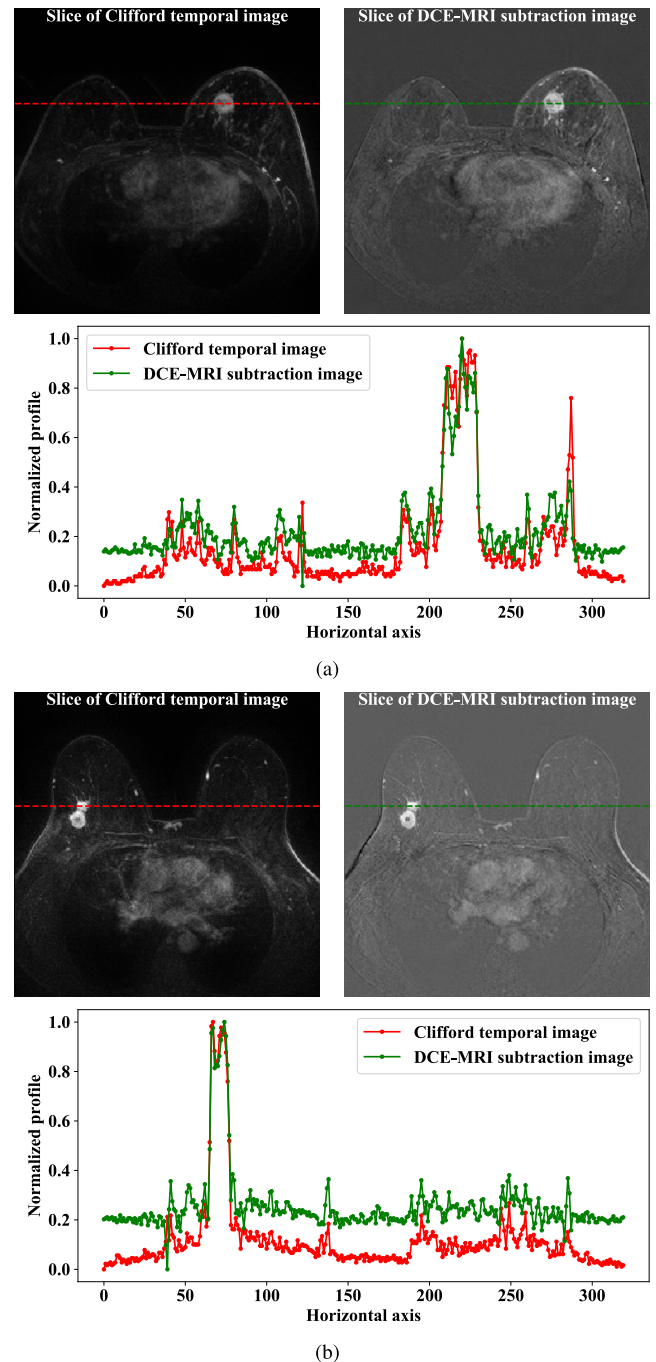


**FIGURE 3.** Two examples from QIN DCE dataset: slices of CTI (upper-left) and DCE-MRI subtraction image (upper-right) and their profiles (bottom). (a) case BC01\_2; (b) case BC10\_1.

For the QIN DCE dataset, there were one pre-contrast time point and about 30 post-contrast time points for a treatment. Each patient had the MRI data of two independent treatments. The MRI data were acquired using a Siemens 3T TIM Trio system on the transverse plane. The transverse plane image size was  $320 \times 320$ , with a pixel spacing of around 1.0 mm. Each sequence had 112~120 transverse plane slices, with a slice spacing of 1.4 mm. The voxel-wise lesion annotations are provided for each treatment. Table 1 shows the details of the two datasets.

**TABLE 1.** Details of adopted datasets.

Dataset name	TBD	QIN DCE
Scanner	Siemens Skyra 3T	Siemens 3T TIM Trio
Case number	224	20
Sequence number of each case	6	32~34
Sequence size (voxels)	$448 \times 448 \times (\sim 80)$	$320 \times 320 \times (112 \sim 120)$
Voxel size (mm)	$0.8 \times 0.8 \times (1.6 \sim 2.0)$	$1 \times 1 \times 1.4$
Number of training cases	184	0
Number of validation cases	20	0
Number of test cases	20	12

### B. EFFECTS OF 3D CLIFFORD TEMPORAL IMAGE

In our experiment, no preprocessing was applied to the DCE-MRI sequences. The CTI  $I_C(x, y, z)$  was computed at all six DCE-MRI time points from the TBD dataset. For the QIN DCE dataset, each study contained more than 20 time points of DCE-MRI sequences, and all were used to compute the CTI. Since the subtraction image is used in conventional methods [16], [19], [21]–[23], the post-contrast sequence at peak enhancement time point and the pre-contrast sequence were used to obtain the best subtraction image in our experiment.

Figure 3 shows two examples of a CTI and DCE-MRI subtraction image on one slice from the QIN DCE dataset. The normalized pixel intensity of a horizontal profile is shown. The background pixel intensity of CTI is clearly lower than that of the DCE-MRI subtraction image. Therefore, better contrast can be obtained by the proposed method.

In addition, to obtain the general performance of the 3D CAS approach for imaging quality improvement, we adopted the structural similarity index (SSIM) [29] for image quality assessment, which simulates human visual perception and is highly adapted for extracting structural information from a scene. The ground-truth lesion segmentations were used as the reference for SSIM. The calculation of SSIM considers image luminance, structure, and contrast [29]. The mean SSIM of the proposed CAS images was compared with that of subtraction images in two scenarios on both datasets: with and without breast mask. Specifically, we calculated SSIM for lesion areas within: 1) only the breast region area; or 2) the entire image. The results are shown in Table 2. It can be observed that the proposed CTI has a higher SSIM than the DCE-MRI subtraction image on both datasets; for example, 0.831 vs 0.827 on QIN DCE, and 0.837 vs 0.830 on TBD. Note that when calculating the SSIM on the entire image (e.g., without breast mask in Table 2), the SSIM value is very small. One of the main reasons could be the strong noises and large highlight volume in the heart area. Above all, the proposed CTI consistently outperforms the subtraction image.

### C. APPLICATION FOR BREAST DCE-MRI LESION SEGMENTATION

For breast lesion segmentation, two successive FCNs were trained. The first FCN (FCN1) was trained for segmentation of the whole breast area, and the second (FCN2) for breast lesion segmentation. Specifically, 3D U-net [30] architecture,

**TABLE 2.** SSIM results form QIN DCE and TBD datasets.

Methods	SSIM with breast mask	SSIM without breast mask
QIN DCE dataset		
Proposed CTI	<b>0.83125</b>	<b>0.00106</b>
subtraction image	0.82731	0.00034
TBD dataset		
Proposed CTI	<b>0.83652</b>	<b>0.00035</b>
subtraction image	0.83064	0.00027

which has attracted considerable attention for superior performance in biomedical image segmentation, was employed for both FCN1 and FCN2. U-net consists of a contracting path to capture context information and a symmetric expansive path that enables precise localization. The contracting path contains three down-convolution blocks, each with two  $3 \times 3 \times 3$  convolutional layers with a rectified linear unit (ReLU) and a  $2 \times 2 \times 2$  max pooling operation with stride 2 for downsampling. The number of feature channels is doubled at each downsampling step. The expansive path has symmetric four up-convolution blocks, each consisting of an upsampling of the feature map followed by a  $2 \times 2 \times 2$  convolution that halves the number of feature channels, and two  $3 \times 3 \times 3$  convolutions, each followed by a ReLU. U-net concatenates the feature maps of each down-convolution block to its corresponding up-convolution block (a.k.a. a skip connection), to recover lost spatial information that can be used by upsampling operations for precise localization.

The input of the FCN1 is a one-channel 3D pre-contrast sequence. The whole breast ROIs were first detected by FCN1 [12]. For more efficient convergence of the FCN2 model, the left and right halves were used to separate the left and right side breast on each of the coronal planes of the detected breast ROI image, thus obtaining a rough single breast 3D ROI to train the FCN2 model.

The input of FCN2 is two-channel data. One channel is the single breast ROI image. The second is the same ROI from CTI,  $I_C(x, y, z)$ . The input data were normalized to  $160 \times 160 \times 160$  with a common spacing resolution to  $0.8 \times 0.8 \times 0.8 \text{ mm}^3$ .

For a fair comparison with existing subtraction image-based methods [16], [19], [21]–[23], the breast ROI and subtraction image were used to train another lesion segmentation FCN network; we call this the DCE-MRI subtraction image-based (DS) method in this paper. In addition, the DeepMedic (DM) method [31] was adopted as a whole chain method for comparison. This method developed a dual pathway multi-scale 3D CNN for lesion segmentation with multi-channel input of MRI data. Its performance has achieved top ranking on the public benchmarks BRATS 2015 [32] and ISLES 2015 [33]. The input of DM consists of two channels: the 3D pre-contrast sequence and the post-contrast sequence at the peak enhancement time point. As DM requested, intensity normalization and voxel size normalization are performed for preprocessing the QIN and TBD datasets. To compare the performance of DM inside the whole breast region, we used the stage-one results of

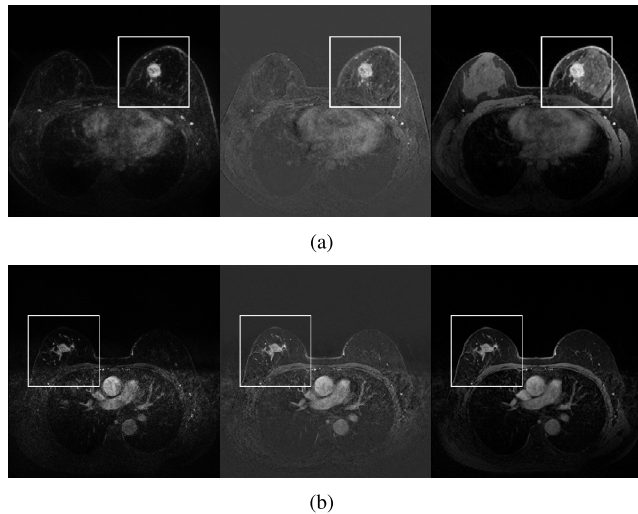


**FIGURE 4.** Example images on the transverse plane with lesion in the indicated ROI. From left to right: proposed CTIs, subtraction images, and post-contrast sequences. (a) case BC01\_2 from QIN DCE dataset; (b) case 1 from TBD test dataset.

the proposed method (the whole breast mask) to filter DM results, enabling the evaluation of false positives of DM in the whole breast region. The DM with whole breast mask is called DM + BM in this paper.

Two examples from the QIN dataset are shown in Fig. 4. From left to right are the proposed CTIs, subtraction images, and post-contrast images, on one transverse plane. An ROI on one side breast indicates the region of lesions. Table 3 shows the quantity segmentation metric in terms of the dice similarity coefficient (DICE) and average symmetric surface distance (ASSD) on the QIN DCE and TBD datasets.

There are 32 test sequences in total, 12 from the QIN dataset and 20 from the TBD dataset. The proposed method obtains an average DICE of 0.813, which is 11.5%, 11.3%, and 8.5% higher than those of DS, DM, and DM + BM, respectively. For the average ASSD results, the proposed method reduces the error by 5.3, 19.9, and 15.4 pixels, respectively, compared to DS, DM, and DM + BM.

The proposed method outperforms the others on each dataset. On DICE, the improvement ranges from 7.3% (0.870 vs. 0.797) against DM + BM on TBD to 17.6% (0.718 vs. 0.542) against DM on QIN. On ASSD, the improvement ranges from 3.64 pixels error (1.445 vs. 5.084) against DS on TBD to 28.62 pixels error (1.667 vs. 30.287) against DM on QIN.

Considering the whole breast region, it can be observed that the average DICE of DM + BM is 2.8% higher than that of DM. This is because several false-positive regions were filtered by the breast mask of the DM + BM method. Although DM + BM is better than DM, the proposed method still has obvious advantages that validate the effectiveness of the combination of CTI and successive FCNs.

Since all the methods were trained using only the TBD dataset, the results on QIN are lower than those on TBD.

**TABLE 3.** Global DICE and ASSD results from QIN DCE and TBD datasets.

Methods	DICE			ASSD (pixels)		
	Average DICE	Dataset QIN DCE	Dataset TBD	Average ASSD	Dataset QIN DCE	Dataset TBD
Proposed	<b>0.813</b>	<b>0.718</b>	<b>0.870</b>	<b>1.528</b>	<b>1.667</b>	<b>1.445</b>
DS	0.698	0.618	0.745	6.831	9.744	5.084
DM	0.700	0.542	0.795	21.455	30.287	16.156
DM+BM	0.728	0.614	0.797	16.998	19.759	15.342

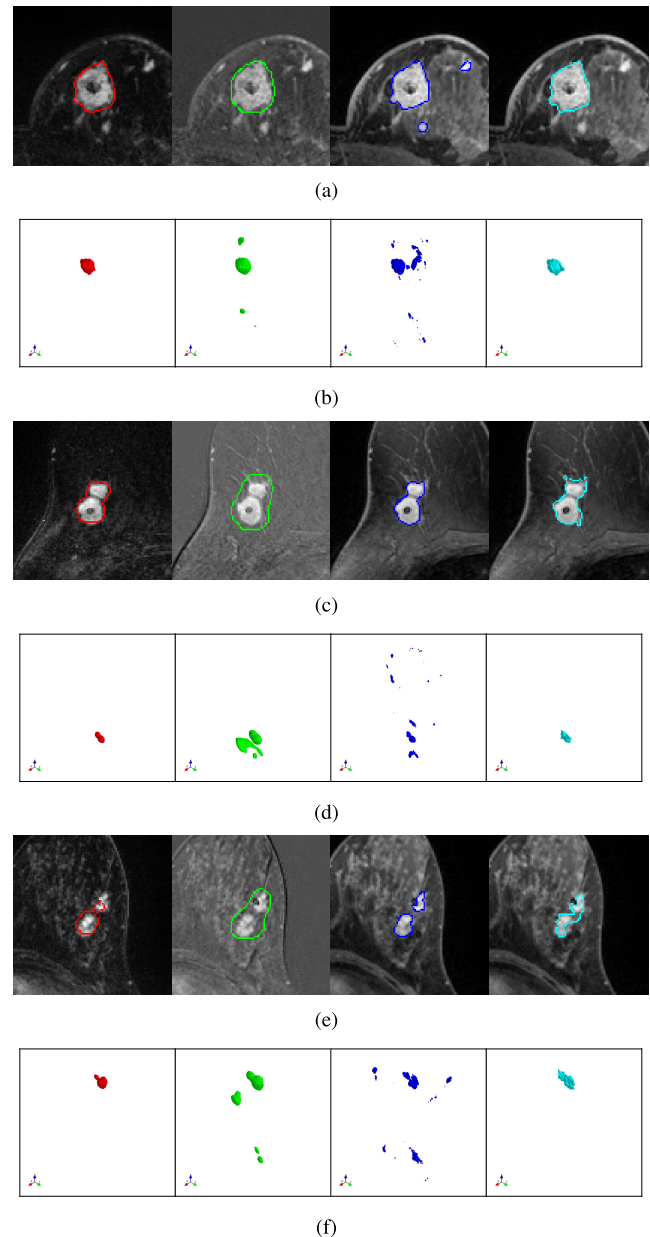


**FIGURE 5.** Lesion segmentation results from QIN DCE dataset on a 2D transverse plane ((a),(c),(e)) and a 3D view ((b),(d),(f)). From left to right: proposed method (red), DS method (green), DM method (blue), and ground truth (cyan). (a)(b) case BC01\_2; (c)(d) case BC10\_1; (e)(f) case BC14\_2.

However, we can observe that the proposed method is more robust than the other methods. From the results of the proposed method, the difference value of DICE between the QIN and TBD datasets (0.870 – 0.718) is lower than that from the



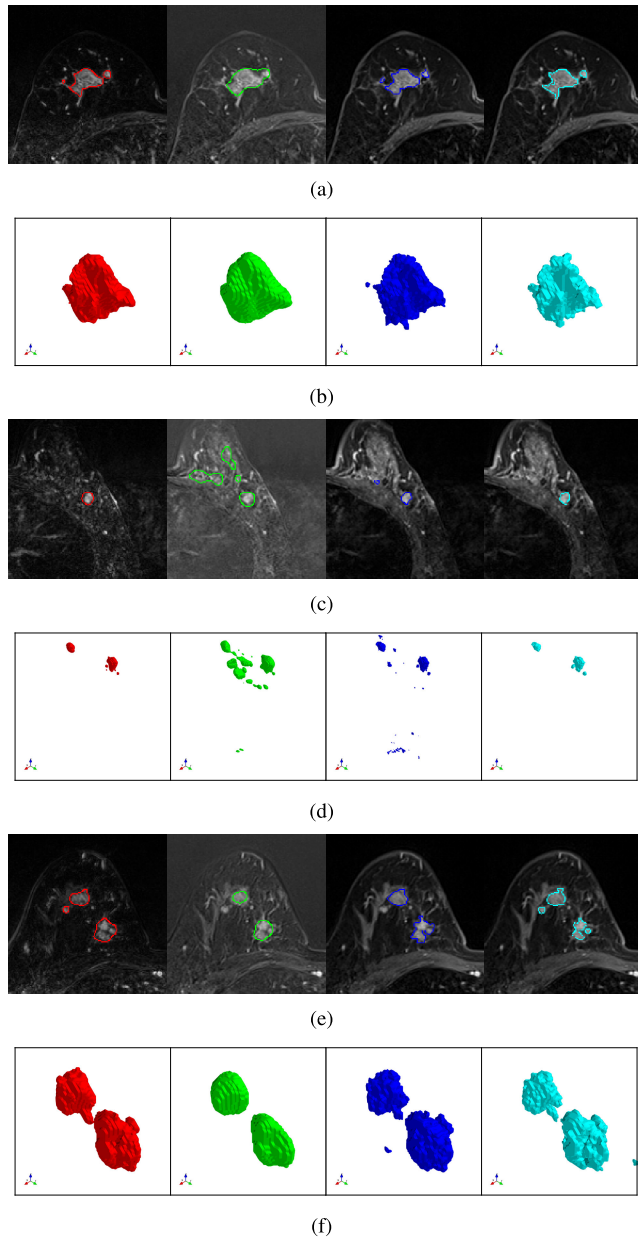


**FIGURE 6.** Lesion segmentation results from TBD test dataset on a 2D transverse plane ((a),(c),(e)) and a 3D view ((b),(d),(f)). From left to right: proposed method (red), DS method (green), DM method (blue), and ground truth (cyan). (a)(b) case 1; (c)(d) case 2; (e)(f) case 3.

DM method (0.795 – 0.542) and from the DM + BM method (0.797 – 0.614), and is similar to that from the DS method (0.745 – 0.618). Moreover, the difference value of ASSD between QIN and TBD datasets from the proposed method (1.667 – 1.445) is much lower than those from all the other compared methods.

Some examples of segmentation results on an ROI of the 2D transverse plane and in a 3D view are shown in Fig. 5 and Fig. 6. The corresponding results of DICE and ASSD of each single case are shown in Table 4. It can be observed that both the DS and DM methods obtain several false positives

**TABLE 4.** Performance of QIN DCE and TBD cases.

Case names	Methods	DICE	ASSD
QIN DCE dataset			
BC01_2	Proposed	<b>0.910</b>	<b>0.766</b>
	DS	0.773	10.669
	DM	0.772	19.919
	DM+BM	0.842	8.390
BC10_1	Proposed	<b>0.804</b>	<b>0.977</b>
	DS	0.268	11.163
	DM	0.627	24.127
	DM+BM	0.641	23.657
BC14_2	Proposed	<b>0.621</b>	<b>1.521</b>
	DS	0.390	23.182
	DM	0.540	42.247
	DM+BM	0.553	42.946
TBD dataset			
Case 1	Proposed	<b>0.910</b>	<b>0.532</b>
	DS	0.806	1.162
	DM	0.883	0.810
	DM+BM	0.884	0.754
Case 2	Proposed	<b>0.866</b>	<b>0.610</b>
	DS	0.435	11.500
	DM	0.850	17.106
	DM+BM	0.854	16.845
Case 3	Proposed	0.871	<b>0.700</b>
	DS	0.830	1.154
	DM	<b>0.872</b>	1.806
	DM+BM	<b>0.872</b>	1.806

(Fig. 5(d) and (f)). Moreover, for the three cases of the TBD dataset in Fig. 6, it can be observed that the NME regions around the lesion ROI are suppressed by the proposed CTI slices (see first column in Fig. 6(c) and (e)), thus avoiding the false positives. The results of the proposed method are closest to the ground truth for both large and small lesions. Above all, the proposed CTI shows good capability in suppressing non-lesion enhancement of the breast DCE-MRI sequences. It therefore enables the segmentation algorithm to obtain a better lesion segmentation result.

#### IV. CONCLUSION

In this work, we proposed a 3D CTI generating method that splits temporal features by using the 3D biquaternion CAS approach. By applying the CTI to 4D spatial-temporal breast DCE-MRI data, the response of non-lesion regions is effectively suppressed. Moreover, by using CTI and two successive FCNs, our method obtains a good accuracy improvement over current methods in the task of lesion segmentation. Future research will improve the lesion segmentation framework by adopting multiple modalities of MRI data. This may be achieved by using a single FCN model with multiple input channels, such as the multi-phase T1-weighted series, T1-weighted nonfat-saturated sequence, T2-weighted sequence, and 3D CTI from multi-b-value diffusion-weighted series.

#### ACKNOWLEDGMENT

(Liang Wang and Haocheng Shen contributed equally to this work.)

#### REFERENCES

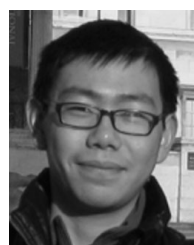
- [1] S. Vinnicombe, “How I report breast magnetic resonance imaging studies for breast cancer staging and screening,” *Cancer Imaging*, vol. 16, no. 1, p. 17, Dec. 2016.



- [2] N. Antropova, B. Huynh, and M. Giger, "SU-D-207B-06: Predicting breast cancer malignancy on DCE-MRI data using pre-trained convolutional neural networks," *Med. Phys.*, vol. 43, no. 6, pp. 3349–3350, Jun. 2016.
- [3] R. Rasti, M. Teshnehlab, and S. L. Phung, "Breast cancer diagnosis in DCE-MRI using mixture ensemble of convolutional neural networks," *Pattern Recognit.*, vol. 72, pp. 381–390, Dec. 2017.
- [4] A. Gubern-Mérida, R. Martí, J. Melendez, J. L. Hauth, R. M. Mann, N. Karssemeijer, and B. Platel, "Automated localization of breast cancer in DCE-MRI," *Med. Image Anal.*, vol. 20, no. 1, pp. 265–274, Feb. 2015.
- [5] R. Adams and L. Bischof, "Seeded region growing," *IEEE Trans. Pattern Anal. Mach. Intell.*, vol. 16, no. 6, pp. 641–647, Jun. 1994.
- [6] W. Chen, M. L. Giger, and U. Bick, "A fuzzy C-means (FCM)-based approach for computerized segmentation of breast lesions in dynamic contrast-enhanced MR images," *Acad. Radiol.*, vol. 13, no. 1, pp. 63–72, Jan. 2006.
- [7] Z. Pang, D. Zhu, D. Chen, L. Li, and Y. Shao, "A computer-aided diagnosis system for dynamic contrast-enhanced MR images based on level set segmentation and ReliefF feature selection," *Comput. Math. Methods Med.*, vol. 2015, Oct. 2015, Art. no. 5308517.
- [8] B. Reig, L. Heacock, K. J. Geras, and L. Moy, "Machine learning in breast MRI," *J. Magn. Reson. Imag.*, to be published, doi: [10.1002/jmri.26852](https://doi.org/10.1002/jmri.26852).
- [9] I. A. Illan, J. Ramirez, J. M. Gorris, M. A. Marino, D. Avendano, T. Helbich, P. Baltzer, K. Pinker, and A. Meyer-Baeke, "Automated detection and segmentation of nonmass-enhancing breast tumors with dynamic contrast-enhanced magnetic resonance imaging," *Contrast Media Mol. Imag.*, vol. 2018, Oct. 2018, Art. no. 5308517.
- [10] L. Zhang, A. A. Mohamed, R. Chai, Y. Guo, B. Zheng, and S. Wu, "Automated deep learning method for whole-breast segmentation in diffusion-weighted breast MRI," *J. Magn. Reson. Imag.*, vol. 10950, Mar. 2019, Art. no. 109502R.
- [11] L. Zhang, Z. Luo, R. Chai, D. Arefan, J. Sumkin, and S. Wu, "Deep-learning method for tumor segmentation in breast DCE-MRI," *Med. Imag.*, vol. 10954, Mar. 2019, Art. no. 109540F.
- [12] J. Zhang, A. Saha, B. J. Soher, and M. A. Mazurowski, "Automatic deep learning-based normalization of breast dynamic contrast-enhanced magnetic resonance images," 2018, *arXiv:1807.02152*. [Online]. Available: <https://arxiv.org/abs/1807.02152>
- [13] P. Herent, B. Schmauch, P. Jehanno, O. Dehaene, C. Saillard, C. Balleyguier, J. Arfi-Rouche, and S. Jégou, "Detection and characterization of MRI breast lesions using deep learning," *Diagnostic Interventional Imag.*, vol. 100, no. 4, pp. 219–225, Apr. 2019.
- [14] C. Gallego-Ortiz and A. L. Martel, "A graph-based lesion characterization and deep embedding approach for improved computer-aided diagnosis of nonmass breast MRI lesions," *Med. Image Anal.*, vol. 51, pp. 116–124, Jan. 2019.
- [15] M. U. Dalmış, S. Vreemann, T. Kooi, R. M. Mann, N. Karssemeijer, and A. Gubern-Mérida, "Fully automated detection of breast cancer in screening MRI using convolutional neural networks," *J. Med. Imag.*, vol. 5, no. 1, Jan. 2018, Art. no. 014502.
- [16] G. Maicas, G. Carneiro, A. P. Bradley, J. C. Nascimento, and I. Reid, "Deep reinforcement learning for active breast lesion detection from DCE-MRI," in *Proc. Int. Conf. Med. Image Comput. Comput.-Assist. Intervent.* Cham, Switzerland: Springer, 2017, pp. 665–673.
- [17] K. He, X. Zhang, S. Ren, and J. Sun, "Deep residual learning for image recognition," in *Proc. IEEE Conf. Comput. Vis. Pattern Recognit. (CVPR)*, Jun. 2016, pp. 770–778.
- [18] V. Mnih, K. Kavukcuoglu, D. Silver, A. A. Rusu, J. Veness, M. G. Bellemare, A. Graves, M. Riedmiller, A. K. Fidjeland, G. Ostrovski, S. Petersen, C. Beattie, A. Sadik, I. Antonoglou, H. King, D. Kumaran, D. Wierstra, S. Legg, and D. Hassabis, "Human-level control through deep reinforcement learning," *Nature*, vol. 518, no. 7540, pp. 529–533, Feb. 2015.
- [19] G. Maicas, G. Carneiro, and A. P. Bradley, "Globally optimal breast mass segmentation from DCE-MRI using deep semantic segmentation as shape prior," in *Proc. IEEE 14th Int. Symp. Biomed. Imag. (ISBI)*, Apr. 2017, pp. 305–309.
- [20] D. Mumford and J. Shah, "Optimal approximations by piecewise smooth functions and associated variational problems," *Commun. Pure Appl. Math.*, vol. 42, no. 5, pp. 577–685, Jul. 1989.
- [21] G. Maicas, A. P. Bradley, J. C. Nascimento, I. Reid, and G. Carneiro, "Pre and post-hoc diagnosis and interpretation of malignancy from breast DCE-MRI," 2018, *arXiv:1809.09404*. [Online]. Available: <https://arxiv.org/abs/1809.09404>
- [22] G. Maicas, G. Snaauw, A. P. Bradley, I. D. Reid, and G. Carneiro, "Model agnostic saliency for weakly supervised lesion detection from breast DCE-MRI," 2018, *arXiv:1807.07784*. [Online]. Available: <https://arxiv.org/abs/1807.07784>
- [23] L. Losurdo, T. M. A. Basile, A. Fanizzi, R. Bellotti, U. Bottigli, R. Carbonara, R. Dentamaro, D. Diacono, V. Didonna, A. Lombardi, F. Giotta, C. Guaragnella, A. Mangia, R. Massafra, P. Tamborra, S. Tangaro, and D. La Forgia, "A gradient-based approach for breast DCE-MRI analysis," *BioMed Res. Int.*, vol. 2018, pp. 1–10, May 2018.
- [24] C. Wachinger, T. Klein, and N. Navab, "The 2D analytic signal for envelope detection and feature extraction on ultrasound images," *Med. Image Anal.*, vol. 16, no. 6, pp. 1073–1084, Aug. 2012.
- [25] L. Wang, A. Basarab, P. R. Girard, P. Croisille, P. Clarysse, and P. Delachartre, "Analytic signal phase-based myocardial motion estimation in tagged MRI sequences by a bilinear model and motion compensation," *Med. Image Anal.*, vol. 24, no. 1, pp. 149–162, Aug. 2015.
- [26] S. J. Sangwine and N. Le Bihan, "Hypercomplex analytic signals: Extension of the analytic signal concept to complex signals," in *Proc. 15th Eur. Signal Process. Conf.*, Poznan, Pologne, 2007, pp. 621–624.
- [27] P. Girard, R. Pujol, P. Clarysse, A. Marion, R. Goutte, and P. Delachartre, "Analytic video (2D + t) signals using clifford-Fourier transforms in multiquaternion grassmann hamilton clifford algebras," in *Quaternion and Clifford Fourier Transforms and Wavelets* (Trends in Mathematics), E. Hitzer and S. J. Sangwine, Eds. Basel, Switzerland: Springer, 2013, pp. 197–219.
- [28] W. Huang et al., "Variations of dynamic contrast-enhanced magnetic resonance imaging in evaluation of breast cancer therapy response: A multicenter data analysis challenge," *Transl. Oncol.*, vol. 7, no. 1, pp. 153–166, 2014.
- [29] Z. Wang, A. Bovik, H. Sheikh, and E. Simoncelli, "Image quality assessment: From error visibility to structural similarity," *IEEE Trans. Image Process.*, vol. 13, no. 4, pp. 600–612, Apr. 2004.
- [30] O. Çiçek, A. Abdulkadir, S. S. Lienkamp, T. Brox, and O. Ronneberger, "3D U-net: Learning dense volumetric segmentation from sparse annotation," in *Proc. Int. Conf. Med. Image Comput. Comput.-Assist. Intervent.* Cham, Switzerland: Springer, 2016, pp. 424–432.
- [31] K. Kamnitsas, C. Ledig, V. F. Newcombe, J. P. Simpson, A. D. Kane, D. K. Menon, D. Rueckert, and B. Glocker, "Efficient multi-scale 3D CNN with fully connected CRF for accurate brain lesion segmentation," *Med. Image Anal.*, vol. 36, pp. 61–78, Feb. 2017.
- [32] B. H. Menze et al., "The multimodal brain tumor image segmentation benchmark (BRATS)," *IEEE Trans. Med. Imag.*, vol. 34, no. 10, pp. 1993–2024, Oct. 2015.
- [33] H.-L. Halme, A. Korvenoja, and E. Salli, "ISLES (SISS) challenge 2015: Segmentation of stroke lesions using spatial normalization, random forest classification and contextual clustering," in *Brainlesion: Glioma, Multiple Sclerosis, Stroke Traumatic Brain Injuries*, A. Crimi, B. Menze, O. Maier, M. Reyes, and H. Handels, Eds. Cham, Switzerland: Springer, 2016, pp. 211–221.



**LIANG WANG** received the French Engineering degree in electronic systems, networks and images from the Ecole Supérieure d'Electricité, in 2010, and the Ph.D. degree from the Institute National des Sciences Appliquées de Lyon (INSA Lyon), France, in 2015. He has been a Senior Engineer with Tencent, since 2017. His research interests include the complex and hyper complex signal in Clifford algebra, medical image processing, and deep learning.



**HAOCHENG SHEN** received the M.Sc. degree in computing with vision and imaging, and the Ph.D. degree in medical image analysis from the University of Dundee, Dundee, U.K., in 2013 and 2018, respectively. He has been a Senior Engineer of AI platform with Tencent, since 2018. His research interests include MR imaging analysis, computer vision, and deep learning.



**JUN ZHANG** received the B.S. and Ph.D. degrees from Xidian University, Xi'an, China, in 2009 and 2014, respectively. He is currently a Research Engineer from Tencent AI Healthcare. His research interests include image processing, machine learning, pattern recognition, and medical image analysis.



**YANCHUN ZHU** received the Ph.D. degree in medical physics from Peking University. He was a Visiting Scholar with Cornell University. He worked with the Shenzhen Institutes of Advanced Technology, Chinese Academy of Sciences and University of California, San Diego, as a Postdoctoral Fellow. He has been a Technique and Research Consultant with Tencent Healthcare, since 2018. He mainly researches on magnetic resonance imaging acquisition techniques, image reconstruction algorithm, and image post-processing algorithm.



**CHENG JIANG** received the B.S. degree in remote sensing science and technology, and the Ph.D. degree in photogrammetry and remote sensing from Wuhan University, Wuhan, China, in 2010 and 2015, respectively. He held a Post-doctoral position with the Institut de Planétologie et d'Astrophysique de Grenoble (IPAG), Saint-Martin-d'Hères, France, from October 2015 to December 2016. Since September 2017, he has been a Senior Engineer with Tencent Company.

His research interests include image fusion, denoising, super-resolution in remote sensing images, high-accuracy DEM for Mars data, and deep learning in medical image processing.

• • •